Magnetic Characterization of 3D Printed Electrical Steels

By
Thang Pham

Advisors:
Dr. Shanelle Foster, Michigan State University
Dr. Annette Mütze, Technische Universität Graz

FINAL REPORT

Submitted to
Austrian Marshall Plan Foundation
in partial fulfillment of the requirements
for the Marshall Plan Scholarship Program

October 3, 2018

Magnetic Characterization of 3D Printed Electrical Steels

Thang Q. Pham*, Shanelle N. Foster*, Annette Mütze†
*Electrical and Computer Engineering, Michigan State University, East Lansing, MI, USA
†Insitut für Elektrische Antriebstechnik und Maschinen, Technische Universität Graz, Graz, Austria

I. INTRODUCTION

Magnetic cores play a key role in the creation of magnetic flux in the air gap of an electric motor. High permeability, high saturation, low hysteresis and eddy current loss are some of the desired magnetic properties for the magnetic core of electric motors [1].

Typically, magnetic cores of electric motors are formed from electrical steel laminations. However, not all machine topologies benefit from laminated magnetic cores, especially when the desired flow of flux is in the stacking direction. In [2], steel laminations are stacked in the axial direction of the tubular linear machine to create the stator iron core. As a result, the flux in the axial direction will encounter higher reluctance compared to the radial direction. This would limit the machine performance. For tubular linear machine in [3], modules are put together to create the entire stator core. Each individual module is made of laminated steel in the radial direction. The flux flows easier in the axial direction, but is then constrained in the radial direction due to the introduction of large airgap in the stator back iron. Other machine topologies such as claw pole and axial flux machines would also benefit from not laminated magnetic cores, [4].

Manufacturing with soft magnetic composites (SMC) is relatively simple and has been used for construction of axial flux motors and tubular linear motors, [4], [5]. SMC has lower loss at high frequencies compared to electrical laminations making it appealing for high speed, high efficiency applications. The 3D flux paths, as enabled by SMC [6], benefit the axial flux motors [7]. The torque density of axial flux fractional horsepower motors is shown to be more than twice that of its radial flux counterpart in [8].

Compared to steel laminations, SMC allows for ease of realization of complex magnetic cores. Casting and molding techniques can be used to form SMC into arbitrary shapes, however, this process may be cost-prohibitive. In addition, SMC has low permeability, which may compromise the size and weight of the magnetic cores, making it difficult to design high power density electric motors.

Additive manufacturing, also known as 3D printing, is capable of building small and large scale parts of any shape. Recent printing technologies also allow additive manufacturing to use a wide range of materials, including ferromagnetic materials. Thus, it is desirable to expand the use of additive manufacturing to create ferromagnetic materials that can be used in electric motors.

Additive manufacturing technologies have been used to build motor cores [9], [10]; however, the magnetic properties of 3D printed cores have not been adequately explored in the literature or engineering practice. Selective laser melting has been investigated for depositing ferromagnetic alloys [11], [12]. With this additive manufacturing technology, the laser power and laser spot size are adjusted to fully melt the powder to develop a highly dense part without post-processing; however, instability in the molten pool can lead to delamination and cracks.

Binder jet printing (BJP) does not use a laser to melt the powder but instead a sintering process is used to burn off the binder and solidify the part. Although post-processing is utilized with this additive manufacturing technology, binder jet printing can be considered a cost-effective technology, [13]. In addition, BJP has been shown to successfully realize permanent magnets. Early attempts at using BJP to produce magnets show that printed magnets can achieve over 90% of the remnant flux value of commercial injection molded bonded magnets, [13]. Successful handling of NdFeB powder in early works shows that BJP can be considered as an alternative approach for printing ferromagnetic materials.

It is well known that microstructural parameters, including grain size, inclusions, and internal stresses, have a strong influence on magnetic properties, [14], [15]. On the other hand, microstructural parameters of printed parts are also directly linked to the 3D printing process, [16]. Thus, for printed ferromagnetic materials it is important that the magnetic characteristics are well understood and linked to the printing parameters.

This proposed project will assess the magnetic properties of 3D printed ferromagnetic materials. The magnetic characterization uses the Ring test, the Epstein Frame, and the Permeameter methods. Section II discusses the current status of additive manufacturing of ferromagnetic materials. The overview of additive manufacturing methods capable of printing ferromagnetic materials is shown in section III. Section IV provides an overview of the BJP process, as well as the description of the printed samples. Experimental setups and results are discussed in Sections V through VIII. Section IX gives an overview on iron losses, and comparison between losses of printed materials and soft magnetic composites. Details of significance analysis using statistical methods are summarized in section X. Relationships and inter-relationships

This work is supported by the Austrian Marshall Plan Foundation, under Marshall Plan Scholarship award number 841 1051 22 19 2017.

between the process parameters and the magnetic properties are determined in Section XI using statistical analysis, following by conclusion in section XII.

II. CURRENT STATUS ON ADDITIVE MANUFACTURING OF FERROMAGNETIC MATERIALS

Ferromagnetic materials play a key role in the creation of the main flux in the air gap of an electric machine. Typically, they are made of cold rolled steel laminations, containing alloys of iron, silicon, nickel, cobalt, and other additives. Steel laminations exhibit high relative permeability, high magnetic saturation, and low specific loss at low frequency, [14]. For high speed applications, eddy current loss associated with high excitation frequency is a concern. As a result, thin laminations with thickness between 0.1-0.3 mm are used to form magnetic cores to reduce the iron losses and improve efficiency. Manufacturing of thin laminated cores comes with challenges. This is added to the performance cost, ie: degradation of magnetic properties, already incurred due to the punching and cutting process [15].

The traditional manufacturing process of laminated cores involves stamping lamination sheets to the desired shapes and stacking them together. This imposes difficulties and challenges when cores with complex geometries are required. For applications that require complicated structure, 3D magnetic flux paths, or volume constraints, the cores can be made of non-conventional materials such as soft magnetic composites (SMC) or amorphous. However, SMC comes with a cost of low permeability and saturation, while amorphous materials incurs high production cost due to the use of boron, niobium, and complex metallurgy process.

In recent years, additive manufacturing has successfully demonstrated the capability of printing complicated ferromagnetic cores with little tooling required. In [17], [18], a rotor core of a synchronous reluctance machine is completely printed with selective laser melting from a commercial powder mixture of Fe, Ni, and Co. A magnetic coupling with honeycomb structure has also been precisely printed, as shown in [19]. This is not feasible using conventional manufacturing method. In [9], plastic and steel layers are alternately printed to create the rotor core of a DC motor to reduce eddy current losses. A commercial fused deposition modeling printer is used to print the cores of a permanent magnet synchronous machine, [10]. Although thermoplastic is used to print the cores, and magnets are manually placed into the rotor cores, the process shows the potential of manufacturing an entire electrical machine in a one single process.

As iron-silicon (FeSi), iron-nickel (FeNi), and iron-cobalt (FeCo) alloys are the most found materials in electrical machines [1], the majority of additive manufacturing for magnetic cores focuses on these materials. Application of additive manufacturing for amorphous materials, due to their high performance magnetic properties have also been investigated, as shown in [20]–[22].

A. Iron-Cobalt

In applications where volume constraints and high torque density are prioritized, iron-cobalt laminations are usually selected. FeCo has the highest magnetic saturation compared to other ferromagnetic materials, thus allowing more flux to flow through less volume of the iron cores [23]. The high saturation level is achieved due to the dense concentration of cobalt being alloyed with iron. In commercial FeCo laminations, Co usually ranges between 15% to 49%. As cobalt is scarce in supply, this dramatically increases the production cost of FeCo compared to other electrical steels. The required annealing and coating processes further add to the cost of manufacturing. In addition, the low workability of FeCo makes it challenging to realize cores of desired shapes.

As a result, reducing the production cost while maintaining the magnetic saturation of FeCo are of high interest among additive manufacturing researchers. So far, successful printing of FeCo is limited to 3D screen printing and laser engineered net shaping technologies. In [24], FeCo fabricated with 3D screen printing has greater saturation and magnetic flux density compared to iron silicon. The high porosity level within the as-built part, however, hinders its saturation and makes it less appealing in magnetic performance compared to commercial FeCo versions. On the other hands, laser engineered net shaping has shown potential in printing FeCo with magnetic saturation being close to conventional FeCo [25]. Saturation, maximum permeability, and coercivity can be further improved when heat treatment is applied to as-built parts. The annealing process promotes the coarse grain size structure within printed part, thus enhances its magnetic properties. Specific loss of printed parts is still much higher than conventional FeCo. However, the ability to tune alloy compositions and printing parameters to reach optimal magnetic performance shows potential with printed FeCo [26].

B. Iron-Nickel

For small high speed machines, FeNi is usually chosen due to its very low iron loss and high relative permeability. Commercial FeNi has the Ni content in the range of 30% to 80%, depending on application requirements. Additive manufacturing of FeNi, as a result, also focuses on these alloy compositions with varying success.

The majority of studies employs laser based process, such as selective laser melting or laser engineered net shaping, to fabricate FeNi alloys. Reported results on fabricated Fe-30%Ni and Fe-80%Ni show that it is possible to achieve magnetic saturation M_s comparable to commercial FeNi, [27]. The magnetic saturation has been found to be significantly influenced by the laser power and the laser scan speed, [28], [29]. These parameters directly impact the grain size and the density of the fabricated parts, which in turns impacts the magnetic saturation. Optimization of these parameters, however, are required for FeNi with different Ni content to achieve optimal M_s value. Optimization of other printing parameters such as laser scan width or number of scan passes may not be necessary as they have been reported to have low influence on M_s, [30].

One of the major issue with fabricated FeNi is the high intrinsic coercivity H_c, whether FeNi is processed with either selective laser melting or laser engineered net shaping. Measured results on coercivity of fabricated FeNi range between

80 A/m to 3000 A/m [12], [31], compared to the coercivity value of 20 A/m or lower usually found in commercial FeNi. High coercivity indicates high losses and negative impacts on relative permeability. Reduction in intrinsic coercivity can be achieved by reducing the porosity level as well as defects in the printed parts. This can be done by optimization of the laser power and laser scan speed as these parameters have direct influence on the cooling rate and exposure time of the molten pool. These in turns impact the defects, porosity, and density levels of printed parts [32]. In addition, reduction of the coercivity may also be achieved by blending V or Mo elements to FeNi alloys [33]. Adding Mo or V can reduce the negative effects of impurities since the added elements can create oxidation with impurities such as nitrogen and oxygen usually found in alloy [34].

C. *Iron-Silicon*

Non-grain oriented FeSi is the most used ferromagnetic materials for electrical machines. As a result, the majority of the work on additive manufacturing focuses on fabricating FeSi. To achieve functional FeSi suitable for electrical machines, printed FeSi needs high permeability, high magnetic saturation, and low iron loss. Selective laser melting is one of the most focused additive manufacturing method for fabricating FeSi. Compared to FeSi lamination steel, relative permeability of printed FeSi using selective laser melting is lower [35]. Applying heat treatment to printed parts can help remove residual stresses which hinders the relative permeability as well as other magnetic properties [36]. In addition, optimization of laser scan speed and power can also lead to printed FeSi with magnetic properties closer to FeSi lamination steel [37]. The nature of SLM method, however, introduces grain elongation in the build direction into fabricated parts. As a result, FeSi fabricated using selective laser melting can have a high amount of magnetic anisotropy [11]. This could hinder the applications of selective laser melting-processed FeSi to only large electrical machines or transformers.

To remove the effect of residual stresses due to the use of laser in selective laser melting, other additive manufacturing techniques that do not use an energy source to melt the powder have also been researched. In [24], printed FeSi is prepared using 3D screen printing and then compared with commercially available FeSi lamination steel. Magnetic induction and relative permeability at low magnetization is comparable to commercial FeSi steel. The high porosity level and low density of the printed FeSi lead to a smaller value of magnetic saturation. In [38], binder jet printing is used to prepare FeSi. Compared to prototype Somaloy, printed FeSi has much higher relative permeability. Iron loss, however, is still a major concerned with printed FeSi.

III. OVERVIEW OF ADDITIVE MANUFACTURING TECHNIQUES

There are many classifications of additive manufacturing techniques but the following technologies have been successfully shown at printing ferromagnetic materials. All of the technologies mentioned are layer based methods, that create parts to match a predefined computer aided design file. In these technologies, an external energy source or binder is applied to the materials to keep the printed part together.

A. *Powder Bed Technologies*

Powder bed technologies include methods that use an energy source, either laser or electron beam, to sinter or melt a selective layer of powder on a build bed. The energy source is characterized by the power level and the scan speed of the energy source, the spacing distance between the scan patterns, the layer thickness, the size and shape of the parent powder. Additionally, these technologies are suitable for a variety of materials such as composites, polymers, metals, and ceramics. There are three major technologies associated with this classification. They are Selective Laser Sintering (SLS), Selective Laser Melting (SLM), and Electron Beam Melting (EBM). In general, these technologies include the interaction between an energy source and the parent powder. The differences between these technologies lie in how the energy is deposited onto the parent powder, the rate of deposition of the energy, and the microstructure of the finished parts [39].

Selective Laser Sintering: Being the earliest method of powder bed technologies, SLS directs the laser beam onto a layer in a short burst. The powder at the laser spot is partially melted. The temperature of the surrounding powder near the sintered part is controlled such that the temperature difference is small. Large temperature difference can lead to stress on the edges around the sintered layer and the finished part. This would lead to defect in the microstructure, and affect the magnetic characteristics of printed ferromagnetic materials.

Selective Laser Melting: To produce parts with higher density, SLM is preferred compared to SLS. SLM uses laser with higher energy level and a smaller spot size to fully melt the powder layer. Since the powder is completely melted unlike in SLS, the finished parts have better porosity level, homogeneity in microstructure, and better surface roughness. Due to the use of higher energy source, there is a higher level of stress around the spot where laser is applied. Distortion, shrinkage, and possible de-lamination of the finished part can also happen in the cooling process, where the liquid to solid transformation occur.

Electron Beam Melting: In EBM method, the metal powder is also completely melted by an electron beam is accelerated and guided to the desired positions by a lens system. Similar to SLM, finished parts with EBM also feature columnar grains in the build direction [40]. In EBM process, displacement of the powder particle from the powder bed can occur due to the repulsive force generated from the interaction between electrons and powder particles. As a result, this additive manufacturing method may require modifications so it can be suitable for processing ferromagnetic materials.

B. *Direct Energy Deposition*

Direct energy deposition technology is a powder feed additive manufacturing method. In this method, the powders are fed through nozzles onto a build bed. During the powder deposition process, inert gas such as argon is used to aid the flow of the powders through the nozzles. A high energy laser beam is directly guided to the powder deposition and melt a single layer of powder or multiple of layers. The power level and the spot size of the laser beam can be controlled; they affect the microstructure of the printed part and thus require a thorough analysis. The build bed can be moved in the x- and y- directions to create the desired cross section that is corresponding to the computer aided design file. The method of powder deposition allows for using multiple materials, and a larger build volume compared to other additive manufacturing techniques.

Upon printing completion, the part which is attached to the build bed is post-processed. This is implemented to reduce the internal stress within the part and improve its characteristics. Unused powder can then be recycled to reduce the cost of printing.

There are several processes related to this technology. They are direct metal deposition (DMD), laser engineered net shaping (LENS), laser cladding (LD), and direct light fabrications. However, only LENS, developed at Sandia National Laboratories, is the most used process for fabricating ferromagnetic materials.

C. Material Extrusions

In this technology, the feedstock materials are heated and deposited layer by layer onto the build platform via nozzles. Similar to other additive manufacturing techniques, the feedstock materials can be either polymers, ceramics, or metals. The nozzles can be arbitrarily controlled in the xy- directions to create the desired part.

The use of multiple nozzles allows for fabrication of different materials. In [41], the method is used to fabricate a magnetic toroidal core with windings on the core using a custom made magnetic paste, and silver paste, respectively.

One of the most common method in this classification is fused deposition modeling (FDM). There are multiple parameters that can affect the properties of printed parts associated with FDM. They can be the scan speed of the nozzles, scan patterns, the heating temperature that is used to melt the feedstock materials, and the diameter of the nozzles. Analysis of the parameters is important to obtain the optimal settings for printing ferromagnetic materials. Compared to powder bed technologies, however, FDM produces parts at a slower speed and accuracy due to the limitation of nozzle radius.

D. Binder Jet Printing

This method is essentially a powder bed technique. However, it does not use an external energy source to melt the powder. In this work, binder jet printing is used to fabricate ferromagnetic materials. Details of the printing process is shown in section IV.

IV. BINDER JET PRINTING PROCESS

A. Printing Overview

Binder Jet Printing is one of the most capable 3D printing processes since it is known to handle a well range of materials, from polymers and ceramics to metals. The method has been successfully used to print stainless steels, permanent magnets, even electrolytic cell [42], and ferromagnetic materials [38]. Binder Jet Printing (BJP) is classified as a powder bed additive manufacturing technique that does not utilize an energy source as in Selective Laser Melting or Electron Beam Melting. Thus, the powder used in the printing process is not melted together but instead bonded together via the use of binder.

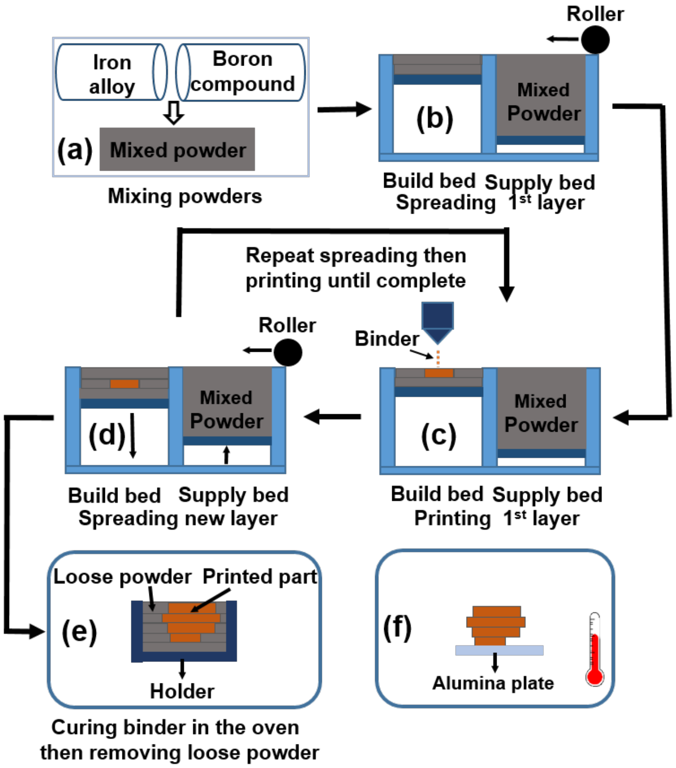

Fig. 1. Binder Jet Printing Process [38].

Binder Jet Printing is a layer by layer manufacturing method that fabricates the part which is created from a computer aided design file. The design file is in STL format and imported into the software of the X1-Lab Printer. The process, as shown in fig. 1, prints each layer in a two-step procedure: powder spreading and binder injection. For each layer, a roller first spreads the powder mixture from the powder bed to the print bed. Binder is injected into predefined parts of each layer, which are indicated by the computer aided design file, in the print bed. The process is repeated until the part is completed. The printed part at this step is also known as the green part.

Upon printing completion, the green part is cured at 195°C for 2 hours to strengthen the binder. It is then cured again at 460°C using the Yamato DX302C Laboratory Drying Oven for another 2 hours to burn off the binder. The cured part is finally placed in an environment-controlled furnace for sintering. To prepare the furnace, air is evacuated from the furnace chamber by the vacuum pump until the pressure reaches 1.33 Pa. Argon gas is then pumped into the furnace chamber until the atmospheric pressure is achieved. The process is repeated prior to the sintering process.

B. Powder Preparation

Off-the-shelf gas atomized iron silicon powders (Fe91Si9) powders, and pure Fe powder are used, as shown in table I. Boron compounds have been proven to enhance sintering by lowering the processing temperature and increase densification [43], so a small amount of boron powder is used as a sintering aid. Printing parameters are chosen due to experience in successful printing of highly dense stainless steel [44].

TABLE I
MATERIALS USED

Powders		**Average Particle Size**
Main Powder	Fe91Si9, Fe	$32\mu m$ $10\mu m$
Sintering additive	B	$1\mu m$

Different powder batches are prepared for printing different samples. A ratio of 75% of the large particle size and 25% of the small particle size, from table I, is used to improve the packing density of the powder mixture. On the other hand, using only large particle size may aid the spreading process since the particles tend to be less lumped together. Only one powder batch has boron added to the powder mixture. The added amount is 0.25% of the powder mixture total mass. Details of the printing batches are discussed in section II-B. The weight of each powder is measured with a high resolution analytical lab scale. The powders are mixed in a high speed mixer, model FlackTek Speed Mixer DAC 150, at 2000rpm and 30s per cycle.

C. Samples Description

Five different samples were printed using five different powder batches. Details of the parent powder composition and the sintering temperature used in the printing process are shown in table II.

TABLE II
BINDER JET PRINTING PARAMETERS.

Sample	Main Powder	Average Particle Size	Sintering Temperature	Additive Compounds
1	Fe$_{91}$Si$_9$	32 μm	1250°C	N/A
2	Fe$_{91}$Si$_9$	26.5 μm	1250°C	N/A
3	Fe$_{91}$Si$_9$	32 μm	1200°C	N/A
4	Fe$_{91}$Si$_9$	26.5 μm	1200°C	N/A
5	Fe$_{91}$Si$_9$ & Fe	26.5 μm	1150°C	0.25% B

The physical properties of the 4 ring specimens are shown in table III. Sample # 5 is printed as several blocks and arranged in the furnace for sintering to form a rod, fig. 2. It is then mechanically cut into twelve different strips, fig. 3, using Electrical Discharge Machining. Their physical properties are shown in table IV. The strips are referred to as Sample # 5 from this point onward.

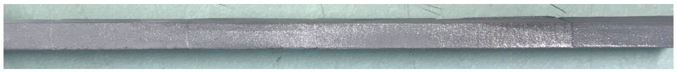

Fig. 2. Binder Jet Printed Iron Silicon Rod/ Specimen # 5.

Fig. 3. BJP Specimen # 5 Mechanically Cut into Strips.

TABLE III
PHYSICAL PROPERTIES OF BINDER JET PRINTED RING SPECIMENS.

Ring	Outer Diameter (mm)	Inner Diameter (mm)
#1	33.99	19.81
#2	34.06	19.89
#3	33.78	19.81
#4	34.04	20.17

TABLE IV
DIMENSIONS AND WEIGHT OF BINDER JET PRINTED STRIPS.

Strip No.	Mean Width (mm)	Mean Thickness (mm)	Mean Length (mm)	Weight (g)
1	13.12	1.04	320.24	32.37
2	13.83	1.04	320.27	32.48
3	13.38	1.04	320.41	32.58
4	13.52	1.02	320.22	32.50
5	13.50	1.04	320.46	32.49
6	13.41	1.04	320.23	32.40
7	13.68	1.05	320.26	32.39
8	13.63	1.04	320.36	31.64
9	12.86	1.02	320.33	29.93
10	12.79	1.00	320.29	30.20
11	13.43	1.04	320.26	32.50
12	13.63	1.04	320.23	32.32

V. EXPERIMENTAL INVESTIGATIONS - GENERAL APPROACH

Magnetic characteristics of the printed samples, including magnetization curves, maximum relative permeability, intrinsic coercivity, and specific loss density are extracted. However, maximum relative permeability, $\mu_{r,max}$, is the main focus of the experiment and the significance analysis.

The magnetic characterization process of the BJP ferromagnetic steels uses three different test setups. They include the Ring Specimen test bed, Permeameter test bed, and Epstein Frame.

The Ring Specimen test bed is used to obtain the magnetization curves and the maximum relative permeability $\mu_{r,max}$ of the ring specimens in table III at low and medium frequencies, following IEC standard [45].

For the printed strips in fig. 3, the Permeameter and the Epstein Frames are used to obtain the magnetic characteristics.

The initial magnetization curve, the hysteresis loop, and the intrinsic coercivity are obtained with the Permeameter, following IEC standard shown in [46]. Using the Epstein Frames, the magnetization curves and the specific loss density curves are acquired following IEC standards for low and medium frequencies, [47], [48].

Table V gives the overview of the experiments used in this work. Details of the experimental setups and results are shown in the following sections.

TABLE V
OVERVIEW OF THE EXPERIMENT TESTBEDS.

	Ring Specimen	Epstein Frames	Permeameter
Sample Type	Rings	Strips	Strips
Excitation Frequency (Hz)	20,50,100 200,400,1000	50, 100 200,400,1000	1
Excitation Range (kA/m)	0-10	0-20	0-20

VI. INVESTIGATION USING RING TEST

A. Setup

The AC characterization, by the use of BJP ring specimens, includes the acquisition of the magnetization curves, and the permeability. Here, the magnetic characteristics are obtained over a range of frequencies from 20 Hz to 1000 Hz, following IEC standard [45].

The overall scheme of the experiment setup is shown in fig. 4. Here, the PAS power amplifier with an output impedance of 50 Ω is used as the source of excitation. Since the amplifier output impedance is large compared to the impedance of the primary windings, distortion of the secondary voltage can easily occur [14]. As a result, current control or sinusoidal magnetic field intensity $H(t)$ is used instead of sinusoidal control on the secondary voltage. To ensure the excitation current conforms to the form factor, a power resistor of 33 Ω is connected in series with the amplifier. Additionally, the built-in function of the amplifier that allows for sinusoidal output is enabled.

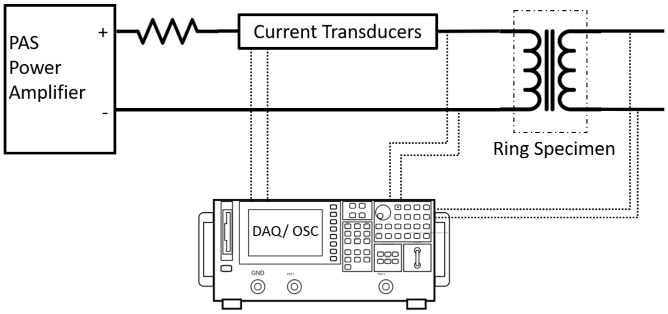

Fig. 4. Experiment Test Setup for Ring Specimens.

The four ring specimens are wound with secondary and primary windings, distributed evenly along the circumference of the ring, as shown in fig. 5. The primary wire gauge is chosen as AWG 20 to ensure that the excitation current can achieve a magnetic field intensity up to 10000 A/m. Higher wire gauge would make it difficult to wind the primary windings without compromising the integrity of the copper strands.

Fig. 5. Binder Jet Printed Ring Specimen with distributed windings.

For each excitation frequency, the magnetization curve is acquired from the excitation current obtained from the current transducer, and the secondary voltage measurement using the oscilloscope. The form factor of the excitation current is checked after every measurement to ensure conformity to the value of $1.11 \pm 1\%$, according to the IEC standard.

The peak magnetic field intensity, $\hat{H}$, is calculated as in (1), from the peak value of the magnetization current, $\hat{I}$, the mean path travel length of the flux, $l_{r,mean}$, and the number of turns in the primary windings of the ring specimen, N_1.

$$\hat{H} = \frac{N_1 \cdot \hat{I}}{l_{r,mean}} \tag{1}$$

Since the ratio of the outer diameter, OD, and inner diameter, ID, of the ring is larger than 1.1, the mean travel length of the flux is corrected as shown in (2).

$$l_{r,mean} = \frac{(OD - ID)}{\ln \frac{OD}{ID}} \cdot \pi \tag{2}$$

The peak magnetic flux density, $\hat{B}$, is calculated from the average rectified value of the secondary voltage, $|\bar{U_2}|$, the number of turns in the secondary windings, N_2, the cross section area of the ring specimen, A_{ring}, and the excitation frequency, f, (3). The relative permeability, μ_r, can then be calculated from $\hat{H}$ and $\hat{B}$.

$$\hat{B} = \frac{|\bar{U_2}|}{4 \cdot f \cdot N_2 \cdot A_{ring}} \tag{3}$$

B. Results

Figure 6 shows the magnetization curves of ring #1 at frequency range from 20 Hz to 1000 Hz. As the excitation frequency increases, the impact of eddy current is more pronounced. It diminishes the induced flux density. This is also seen at low excitation frequency and low magnetization field. The behavior is due to the opposing field generated by the eddy current in the samples [14].

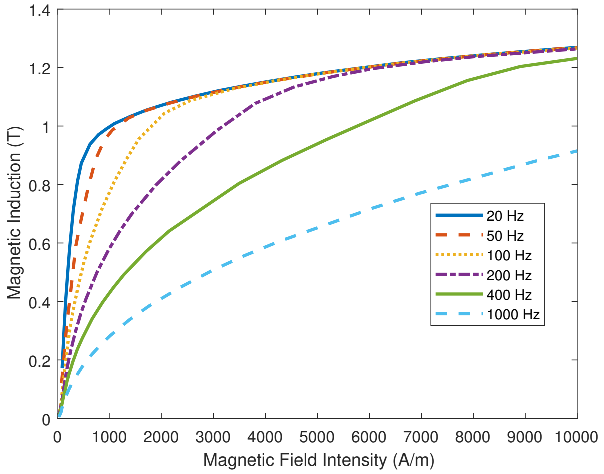

Fig. 6. Ring #1 magnetization curves, obtained at different excitation frequencies. High excitation frequency leads to high eddy current, negatively impact the induced magnetic flux density. The effect is profound at low magnetic field intensity and high frequency.

Figure 7 shows the relative permeability curves of all the ring specimens in table III, at 20 Hz excitation [1]. Since $\mu_{r,max}$ is the focus of this project, $\mu_{r,max}$ is calculated from the magnetization curves at 20 Hz. This minimizes the impact of eddy current on $\mu_{r,max}$, which is later used in the significance test. For each ring, two measurements are obtained in order to satisfy the minimum requirements for the significance test. Table VI summarizes the $\mu_{r,max}$ values for each ring.

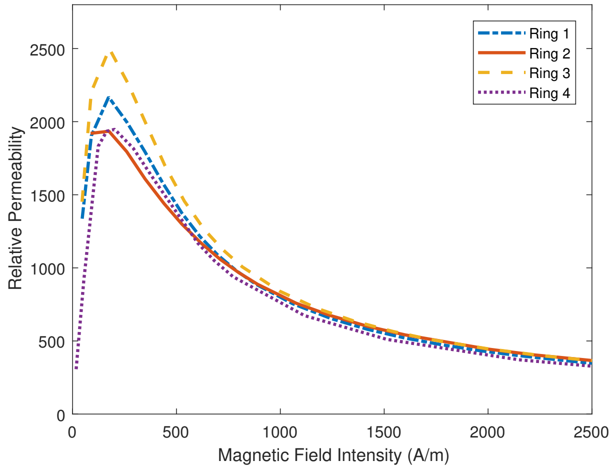

Fig. 7. Comparison between relative permeability curves of the printed ring specimens. The excitation frequency is at 20 Hz.

Maximum relative permeability is highest with ring #3 and lowest with ring #2, as shown in table VI. This is expected, as an increase in particle size results in an increase in relative permeability. It is also interesting that lowering the sintering temperature also leads to an increase in the relative permeability of printed samples. Sensitivity analysis will be carried out to determine the significance of the two parameters involved in the printing process.

TABLE VI
COMPARISON BETWEEN MAXIMUM RELATIVE PERMEABILITY OF BINDER JET PRINTED RING SPECIMENS. DATA AT 20 HZ.

Ring Number	Maximum Relative Permeability	
	Observation 1	Observation 2
#1	2168	2136
#2	1935	1772
#3	2499	2330
#4	1959	1948

TABLE VII
COMPARISON BETWEEN MAGNETIC INDUCTION OF BINDER JET PRINTED RING SPECIMENS. DATA AT 20 HZ.

Ring Number	Magnetic Induction (T)		
	1000 A/m	2500 A/m	10000 A/m
#1	0.99	1.09	1.27
#2	1.01	1.14	1.34
#3	1.05	1.14	1.32
#4	0.935	1.02	1.16

Table VII summarizes the magnetic induction of all the ring specimens at several magnetic field intensity values. Magnetic induction of ring #2 and ring #3 are high compared to the other two ring specimens. Ring #4 has the lowest magnetic induction among all the ring samples. Future analysis of the printing parameters can provide an optimal parameter settings for the magnetic induction of binder jet printed ferromagnetic materials.

VII. INVESTIGATION USING EPSTEIN FRAME

A. *Setup*

The printed strips in table IV are measured using the Epstein Frames to acquire the maximum relative permeability, magnetization curves, and the specific loss density. The twelve strips are evenly distributed into four legs of the Epstein Frames, with each leg having three strips. For excitation frequencies of 50, 100, 200, and 400 Hz, the magnetic characterization is carried out on the EP 700 Frame. The characterization at 1000 Hz is implemented using the medium frequency EP 100 Frame. The parameters for the Epstein Frames, as well as for the measurement devices, are shown in table VIII. Here, R_i is the equivalent resistance of all measuring devices across the secondary windings, R_t is the series impedance of the secondary and compensation windings. N_1 and N_2 are the number of turns in the primary and secondary windings, respectively.

TABLE VIII
PARAMETERS OF EPSTEIN FRAMES AND MEASURING DEVICES.

	N_1	N_2	R_t (Ω)	R_i (Ω)
EP700	700	700	16.5	5e6
EP100	100	100	1.97	5e6

The experimental setup is shown in fig. 8. The power amplifier is controlled to achieve sinusoidal voltage on the

---

[1] Ring #1, #2, and #3 were magnetically characterized at TU Graz. Ring #4 was magnetically characterized at Michigan State University. The two experiment test beds for measuring the four rings are the same in principles. Primary current is sinusoidally controlled. Number of turns in the primary and secondary windings are the same between the rings.

secondary windings in accordance to the desired form factor. This is implemented via the sense lines connected to the primary windings of the Epstein Frames. A power analyzer is used to measure the primary current, the primary and the secondary voltage, and the active power. Measured data are logged and post-processed to acquire the magnetization curve as well as the loss density at each excitation frequency.

Each sample is demagnetized before characterization. The power amplifier is controlled to provide a sinusoidal pulse with its amplitude decreasing to zero in less than 10 s.

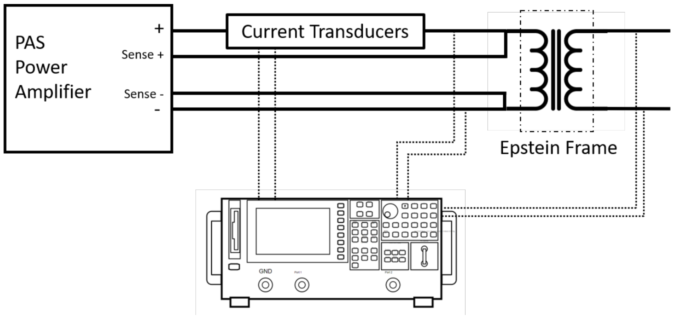

Fig. 8. Epstein Frame Test Setup.

B. Results

As shown in the magnetization curves in fig. 9, at a magnetization field of 20 kA/m, the magnetic induction settles at 1.54 T. As the excitation frequency increases, the magnetic induction is decreased for the same magnetization field. This is due to the opposing field generated by eddy currents associated with high frequency excitation. The behavior is more pronounced at low magnetization field, when comparing the magnetic induction at 50 Hz and at 1000 Hz. This is also observed in the relative permeability curves in fig. 10.

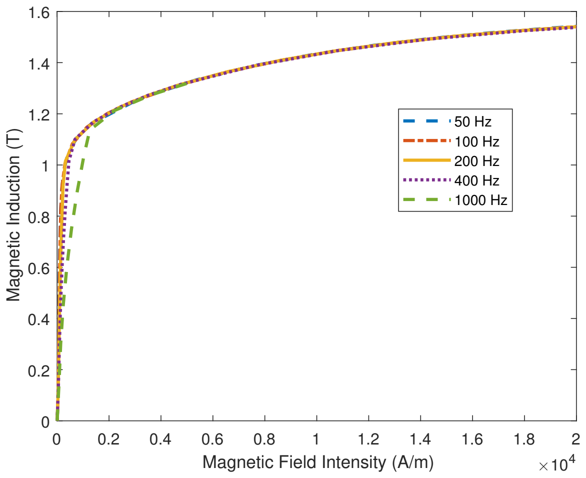

Fig. 9. Magnetization curves of Binder Jet Printed Sample # 5.

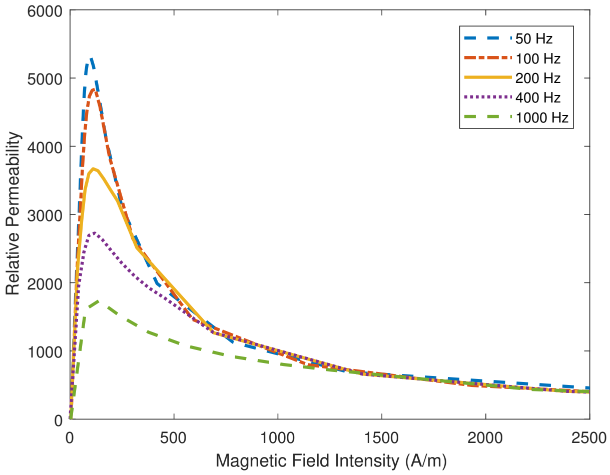

Fig. 10. Relative permeability curves of Binder Jet Printed Sample # 5.

Specific loss of Specimen # 5 is calculated using (4). Here, P_m represents the active power of the magnetization current, $I_1(t)$, and the secondary voltage, $U_2(t)$, measured using the wattmeter. The specific loss density, p_c, is the ratio between P_c and the effective mass of the strips. The effective mass, m_a, is calculated using (5), where l_m is the effective length of the Epstein Frame (0.94 m), l is the average length of the strips in each leg of the Epstein Frame, and m is the total mass of all the strips.

Figure 11 shows the specific loss density curves of Specimen # 5. As the frequency increases, the specific loss increases at an exponential rate. A summary of the specific loss density of the printed materials is shown in table IX.

$$P_c = \frac{N_1}{N_2}P_m - \frac{1.111 \cdot |\bar{U_2}|^2}{R_i} \tag{4}$$

$$m_a = \frac{m \cdot l_m}{4 \cdot l} \tag{5}$$

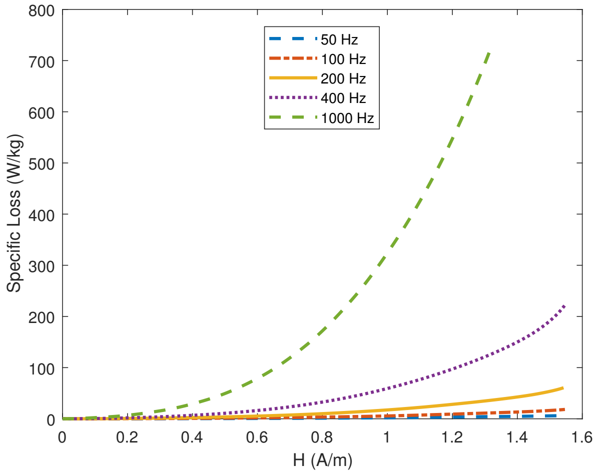

Fig. 11. Specific Loss Density of BJP Specimen # 5 at different frequencies.

VIII. INVESTIGATION USING PERMEAMETER

A. Setup

The experiment setup, fig. 12, consists of a type B permeameter, [49], a fluxmeter, and a power amplifier controlled via

TABLE IX
SPECIFIC LOSS DENSITY IN W/KG OF BJP SPECIMEN # 5.

		Frequency				
		50 Hz	100 Hz	200 Hz	400 Hz	1000 Hz
B	0.5 T	0.51	1.31	3.66	10.81	49.42
	1.0 T	2.07	5.59	17.33	59.24	324.1
	1.5 T	5.71	16.23	53.57	191.25	N/A

LabVIEW. The permeameter has two magnetization windings, and two measurement coils, one for measuring the magnetic field strength, H, and one for the polarization, J, fig. 13. The magnetic induction, B, is calculated from the measurements of the two coils using the relationship $B = J + \mu_0 H$.

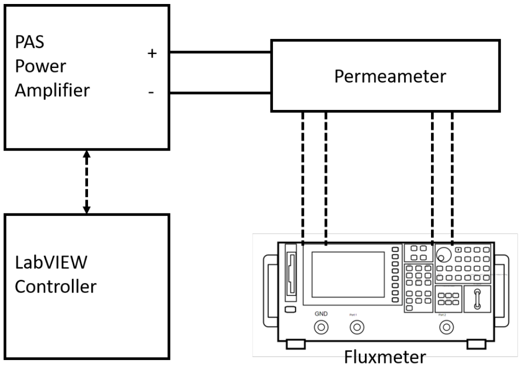

Fig. 12. Permeameter Experiment Setup.

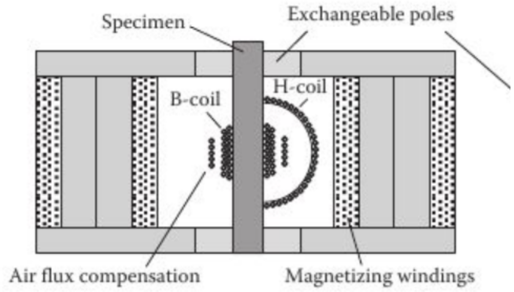

Fig. 13. Type B Permeameter, [49].

Prior to the excitation process, the controller demagnetizes the printed strip to be measured. The controlled power amplifier then provides sinusoidal excitation at 1 Hz to the magnetizing windings of the Permeameter. When the excitation frequency is very low, specifically lower than the Wolman frequency, the eddy current effect can be neglected, [14], [49]. As a result, the magnetization curve is quasi-static and slightly different than the static curve, [15].

B. Results

Figure 14 shows the hysteresis loop and the initial magnetization curve of the printed ferromagnetic strip. The intrinsic coercivity H_{ci} of 56.5 A/m is obtained from the intersection of the hysteresis loop and the horizontal axis. It is worth noting that the H_{ci} value of printed steel strip is smaller than the coercivity values of some commercial lamination steels and soft magnetic composites [50]–[52]. As a result, the hysteresis loss of the printed steel strips in table IV is highly competitive with certain commercial electric steels and SMC.

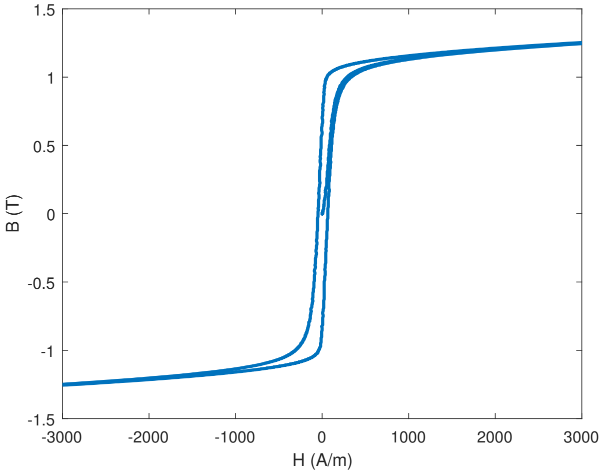

Fig. 14. Initial Magnetization Curve and Hysteresis Loop of Specimen # 5.

Figure 15 shows the initial magnetization curve obtained using the Permeameter. The curve closely tracks the magnetization curves obtained using the Epstein Frames.

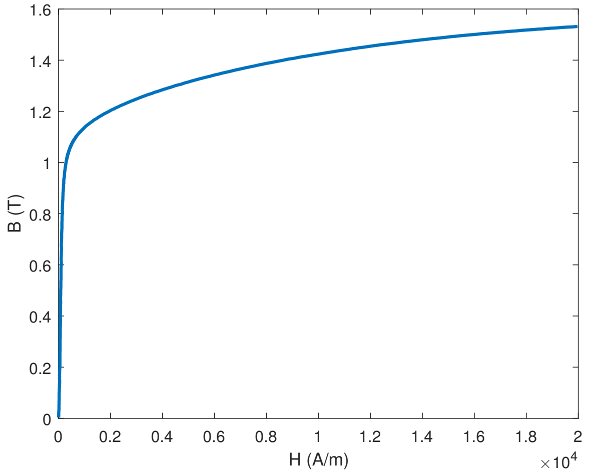

Fig. 15. Initial Magnetization Curve of Specimen # 5 obtained with the Permeameter.

IX. DISCUSSION ON SPECIFIC LOSS DENSITY

A. Overview

The iron loss in ferromagnetic materials comes from the difference in the phase shift between the magnetization field H and the magnetic flux density B, and is calculated over one electrical cycle T, [14]. There are two main components contributing to the iron loss, hysteresis loss, p_h, and eddy loss, p_e. The hysteresis loss is directly related to the coercivity H_c of the materials and is estimated as in (6), where γ is the density of the materials.

$$p_h = \frac{4 \cdot f \cdot H_c \cdot \hat{B}}{\gamma} \tag{6}$$

For a sinusoidal magnetic flux density waveform with form factor value of 1.11, the eddy loss can be approximated as in (7). Here, d represents the thickness of the lamination sheet and ρ is the electrical resistivity of the materials.

$$p_e = \frac{\pi^2 \cdot f^2 \cdot \hat{B}^2 \cdot d^2}{6 \cdot \gamma \cdot \rho} \tag{7}$$

From (6) and (7), it is possible to separate the hysteresis loss from eddy loss by extrapolating the iron loss per cycle, p_{fe}/f, when the excitation frequency approaches 0.

For medium excitation frequency, from 20 to 100 kHz, the specific loss can no longer be estimated as the sum of the relationships in (6) and (7). It is instead estimated using the Steinmetz equation as shown in (8). The values of x, y, z, f_0, $\hat{B}_0$, and F_0 are usually found experimentally.

$$p_{fe} = p_0 \cdot \left(\frac{F}{F_0}\right)^x \cdot \left(\frac{f}{f_0}\right)^y \cdot \left(\frac{\hat{B}}{\hat{B}_0}\right)^z \tag{8}$$

It is important to note that the eddy current loss calculated as in (7) assumes that the permeability is uniform and homogeneous within the materials, [14]. In cases where the change of magnetization dB/dt is much higher in a local area where the moving domain wall locates, then there exists an additional losses. This anomalous eddy loss contributes to the eddy loss, and is usually referred to as excess loss, p_{excess}. The specific loss density is now the sum of the hysteresis loss, the classical eddy loss, and the excess loss as shown in (9).

$$p_{fe} = p_h + p_{e,classical} + p_{excess} \tag{9}$$

As shown in [53], the excess eddy loss of the materials can be estimated as in (10). Here c represents the scaling factor of the specific domain wall energy, [53]. From (9), the hysteresis dominates total iron loss at low excitation frequency. As the excitation frequency increases, the classical eddy loss and the excess loss take over the hysteresis loss and become the dominant factor.

$$p_{excess} = \frac{c \cdot (\hat{B} \cdot f)^{1.5}}{\gamma} \tag{10}$$

B. *Comparison with Prototype Somaloy*

The measured specific loss density of printed ferromagnetic specimen # 5 is very encouraging, table X. It is much lower than the value of prototype somaloy, [52], at up to frequency of 400 Hz and magnetic flux density of $B = 1.0T$. At low excitation frequency, the specimen # 5 can be 2 times lower than the prototype somaloy. One of the contribution to this high performance in printed materials can be explained due to lower hysteresis loss. Although the hysteresis loss of specimen # 5 is not calculated, its intrinsic coercivity is a quarter of somaloy. This indicates lower hysteresis loss since the loss is proportional to the coercivity value, as shown in (6).

Printed materials, however, performs poorer than somaloy at high excitation frequency. This can be explained by the high resistivity of somaloy, which in turns leads to lower eddy current losses. However, this behavior is expected since high resistivity is one of the main advantage of SMC in general.

TABLE X
COMPARISON BETWEEN SPECIFIC LOSS DENSITY OF BINDER JET PRINTED SPECIMEN # 5 AND PROTOTYPE SOMALOY. DATA ARE IN W/kg.

		Frequency				
		50 Hz	100 Hz	200 Hz	400 Hz	1000 Hz
Specimen #5	0.5 T	0.51	1.31	3.66	10.81	49.42
	1.0 T	2.07	5.59	17.33	59.24	324.1
	1.5 T	5.71	16.23	53.57	191.25	N/A
Somaloy	0.5 T	1.6	3.1	6	14	39
	1.0 T	5.2	11	22	47	136
	1.5 T	11	22	45	96	284

X. SIGNIFICANCE ANALYSIS OVERVIEW

A. *Overview of Single Factor Analysis of Variance*

Analysis of Variance (ANOVA) is one of the most useful technique in statistic since it provide an objective view of the analysis of collected data [54]. There are mainly two types of analysis, single factor and multi-factor, which is also known as factorial designs.

In the single factor analysis of variance, it is important to compare the significance of different levels within that factor. Assuming that there are m different levels of the factor under interest; for each level of factor, there is a total of n measurements or observations. The model of all the collected data is shown in (11). Here, y_{ij} represents the j^{th} observed data point at the i^{th} level of the factor under interest; μ_i is the mean value of the i^{th} level of the factor, and ϵ_{ij} is the random error component that is coming from variation in measurements, test materials, and environmental noise. It is assumed that the errors has zero mean value, with constant variance σ^2, and the errors are normally distributed [54]. Equation (12), in which τ_i is called the i^{th} treatment effect, is used to demonstrate that the observed data point y_{ij} is independent from each other.

$$y_{ij} = \mu_i + \epsilon_{ij} \tag{11}$$

$$y_{ij} \sim N(\mu + \tau_i, \sigma^2) \tag{12}$$

For single factor analysis of variance, it is important to test whether each level of the factor has equal impact or not. This is usually described using hypotheses in (13), where H_0 means that all the levels within the factor has the same significant level while H_a means at least one pair of levels has different impact on the output.

$$\begin{aligned} H_0 &: \mu_1 = \mu_2 = ... = \mu_m \\ H_a &: \mu_i \neq \mu_j \end{aligned} \tag{13}$$

The single factor ANOVA includes calculation of the sum of squares of the factor, $SS_{Treatment}$, the sum of squares of the error, SSE, the total sum of squares, SST, mean squares, MS, and F_0 value. The total sum of squares, as shown in (14), is used to determine the total variability in the observed measurements. Here, $\bar{y}_{..}$ is the mean of all of the averages of each level of the factor or $\bar{y}_{i.}$. In other words, $\bar{y}_{i.}$ means the average of n observations within the i^{th} level of the single factor under interest.

$$SST = \sum_{i=1}^{m}\sum_{j=1}^{n}(y_{ij} - \bar{y}_{..})^2 \tag{14}$$

The sum of squares of the error is calculated as in (15) and is related to the total sum of squares as in $SST = SS_{Tr} + SSE$. Once the sum of squares are calculated, the mean squares of the single factor and of the error can be calculated as in (16), where N is the total number of observations/ measurements for all of the levels of the single factor.

$$SSE = \sum_{i=1}^{m}\sum_{j=1}^{n}(y_{ij} - \bar{y}_{i.})^2 \tag{15}$$

$$\begin{aligned} MS_{Tr} &= \frac{SS_{Tr}}{m-1} \\ MSE &= \frac{SSE}{N-m} \end{aligned} \tag{16}$$

Following the Cochran's theorem, the null hypothesis in (13) can be evaluated by applying the test statistic on the ratio of MS_{Tr} and MSE. Assuming that the ratio, F_0, is an F distribution with $m-1$ and $N-m$ degrees of freedom, then the null hypothesis is rejected if $F_0 > F_{\alpha,m-1,N-m}$.

B. Overview of Factorial Designs

For factorial designs or multi-factor statistical analysis, it is important to study the significance of all combinations of the factors under interest. Assuming that there are two factors under interest, A and Y, associated with m and n different levels, respectively, then there is a total of $m \cdot n$ combinations worth investigating.

$$y = \beta_0 + \beta_1 x_1 + \beta_2 x_2 + \beta_{12} x_1 x_2 + \epsilon \tag{17}$$

ANOVA for factorial design focuses on the main effects, which are the impacts of the main factors in the design, and the crossed effects, which represents the interactions between the main factors. For a two factor factorial design, a regression model as shown in (17) is used to demonstrate the effect of the interactions. Here, x_1 describes factor A, x_2 describes factor B, $x_1 x_2$ describes the interaction between the two factors, and ϵ denotes the random error factor associated with the measurements. It is important to note that the values x_1 and x_2 range from -1 to 1. All the parameters of the regression model, β_1, β_2, and β_{12}, are calculated using least squares estimates from all of the observations or measurements.

Similar to (11), the effect model of a two-factor factorial design is described as in (18). Here, μ is the overall mean of the effect y_{ijk}, τ_i is the effect of the i^{th} level of factor A ranging from 1 to m, β_j is the j^{th} effect of factor B ranging from 1 to n. Also, k represents the k^{th} measurement of each combination of the two factors. Assuming that there are p number of measurements for each combination, there is a total of $m \cdot n \cdot p$ observations associated with the factorial design.

$$y_{ijk} = \mu + \tau_i + \beta_j + (\tau \cdot \beta)_{ij} + \epsilon_{ijk} \tag{18}$$

The relationship between the all the sums of squares are described as $SST = SS_A + SS_B + SS_{AB} + SSE$. Here, SS_A is the sum of squares related to the factor A; SS_B is the sum of squares related to the factor B; SSE is the sum of squares due to the error in measurements; and SS_{AB} represents the sum of squares of the interaction. The degrees of freedom associated with the factors, the interaction, and the error terms are $m-1$, $n-1$, $(m-1)\cdot(n-1)$, and $m \cdot n \cdot (p-1)$, respectively. The degree of freedom of the total effect is $m \cdot n \cdot p - 1$.

In concept, the sum of squares, as shown in (19), and the mean squares are calculated similarly to those in the single factor ANOVA. Here, $y_{...}$ represents the sum of all of the observations or measurements, $y_{i..}$ represents the sum of all of the observations/ measurements of the i^{th} level of factor A, $y_{.j.}$ represents the sum of all the observations of the j^{th} level of factor B, $y_{ij.}$ denotes the sum of all of the observations/ measurements for each ij combination.

$$\begin{aligned} SST &= \sum_{i=1}^{m}\sum_{j=1}^{n}\sum_{k=1}^{p} y_{ijk}^2 - \frac{y_{...}^2}{mnp} \\ SS_A &= \frac{1}{np}\sum_{i=1}^{m} y_{i..}^2 - \frac{y_{...}^2}{mnp} \\ SS_B &= \frac{1}{mp}\sum_{j=1}^{n} y_{.j.}^2 - \frac{y_{...}^2}{mnp} \\ SS_{AB} &= \frac{1}{p}\sum_{i=1}^{m}\sum_{j=1}^{n} y_{ij.}^2 - \frac{y_{...}^2}{mnp} - SS_A - SS_B \end{aligned} \tag{19}$$

Considering that the errors has zero mean value, with constant variance σ^2, and the errors are normally distributed [54], then factors A, B, and interaction AB has no impact if the mean squares are also estimated as σ^2. However, there is a significant presence of factors A, B, or interaction AB if the related mean square values are larger than the error mean squares, and larger than the $F_{\alpha,DF,m\cdot n\cdot(p-1)}$, where DF can be $m-1$, $n-1$, or $(m-1)(n-1)$, respectively.

XI. SIGNIFICANCE ANALYSIS RESULTS

Analysis of Variance is implemented in this work to determine the significance of the printing parameters toward the maximum relative permeability of printed ferromagnetic materials. The two parameters are the sintering temperature, T_s, and the average particle size, APS. The significance impact of each parameter is determined first, using Single Factor ANOVA. The significance of the interaction between the two parameters is then determined using the Two Factor ANOVA. It is important to note that the Two Factor ANOVA also provides the significance impact of individual input parameters.

A. Single Factor Analysis of Variance

Table XI summarizes the maximum permeability of all of the ring samples. Two observations are associated with each

TABLE XI
MAXIMUM PERMEABILITY OF SAMPLES AT DIFFERENT AVERAGE PARTICLE SIZE AND SINTERING TEMPERATURE.

	Average Particle Size			
Sintering Temperature	26.5 μm		32 μm	
	Obs. 1	Obs. 2	Obs. 1	Obs. 2
1200C	1959	1948	2499	2330
1250C	1935	1772	2168	2136

ring. At least two observations are required to implement the ANOVA for the input parameters.

The significance of the sintering temperature T_s is determined first. For each APS level, the F_0 value is calculated to test the null hypothesis H_0 against the alternative hypothesis H_a, as shown in (20). Here, H_0 means that sintering temperature at different temperature has no influence on $\mu_{r,max}$. H_a means that sintering temperature actually impacts $\mu_{r,max}$.

Assume a significance level $\alpha = 0.1$, the sintering temperature is said to have an impact on $\mu_{r,max}$ or the null hypothesis is rejected when the F_0 value exceeds $F_{\alpha,1,2} = 8.526$. Table XII shows the single factor ANOVA table associated with the sintering temperature. Here, the F_0 values show that sintering temperature has an impact on $\mu_{r,max}$ when the average particle size is of 32 μm but not when the size is 26.5 μm. Increasing the degree of freedom for the sintering temperature as well as the number of observations can lead to a more definitive conclusion on the effect of sintering temperature.

$$\begin{aligned} H_0 &: \mu_{1200^\circ\text{C}} = \mu_{1250^\circ\text{C}} \\ H_a &: \mu_{1200^\circ\text{C}} \neq \mu_{1250^\circ\text{C}} \end{aligned} \tag{20}$$

The significance of the average particle size is evaluated next. The null hypothesis H_0 is tested against the alternative hypothesis H_a as shown in (21). Both the F_0 values in table XIII exceed $F_{\alpha,1,2} = 8.526$. As a result, the null hypothesis H_0 is rejected. The average particle size is determined to have an impact on $\mu_{r,max}$.

$$\begin{aligned} H_0 &: \mu_{26.5\mu m} = \mu_{32\mu m} \\ H_a &: \mu_{26.5\mu m} \neq \mu_{32\mu m} \end{aligned} \tag{21}$$

TABLE XII
ANOVA TABLE FOR SINTERING TEMPERATURE.

Source of Variation	Degrees of Freedom	F_0
Sintering Temperature @ APS 26.5 μm	1	1.49
Sintering Temperature @ APS 32 μm	1	9.31
Error	2	

TABLE XIII
ANOVA TABLE FOR AVERAGE PARTICLE SIZE.

Source of Variation	Degrees of Freedom	F_0
Average Particle Size @ T_s 1200°C	1	29.64
Average Particle Size @ T_s 1250°C	1	12.92
Error	2	

B. Two Factor Analysis of Variance

The two input parameters have two levels each. Each printed ring specimen represents a combination of the four factorial designs. The significance of the interaction between the input parameters is determined using the Two Factor ANOVA, as shown in table XIV. Here, three F_0 values are calculated to test the significance of the Sintering Temperature, the Average Particle Size, and the Interaction between them. When the F_0 value exceeds $F_{\alpha,1,4}$, the null hypotheses in (22) are rejected. Here, H_{03} means there is no interaction between sintering temperature T_s and the average particle size APS.

$$\begin{aligned} H_{01} &: \mu_{1200^\circ\text{C}} = \mu_{1250^\circ\text{C}} \\ H_{02} &: \mu_{26.5\mu m} = \mu_{32\mu m} \\ H_{03} &: (\mu_{T_s} \cdot \mu_{\text{APS}})_{ij} = 0 \text{ for all i,j} \end{aligned} \tag{22}$$

TABLE XIV
ANOVA TABLE FOR TWO FACTOR - SINTERING TEMPERATURE AND AVERAGE PARTICLE SIZE.

Source of Variation	Degrees of Freedom	F_0
Sintering Temperature	1	9.34
Average Particle Size	1	41.00
Interaction	1	1.88
Error	4	

Assuming the significance level $\alpha = 0.1$, both the Sintering Temperature and the Average Particle Size do have an impact on $\mu_{r,max}$. Their F_0 values both exceed $F_{\alpha,1,4} = 4.5447$. The results from the Two Factor ANOVA are more conclusive than the results of the Single Factor analysis. This is due to higher degree of freedom in the error, which in turns provides more certainty in the significance test.

There is no indication of cross-effect between the two printing parameters. In other words, effect of average particle size and sintering temperature on maximum relative permeability are independent from each other, as the F_0 value of the interaction is much smaller than $F_{\alpha,1,4}$.

It is also interesting to note that the F_0 value of the average particle pize is a multiple of the F_0 value of the sintering temperature. The average particle size, thus, has a higher impact on $\mu_{r,max}$ compared to the sintering temperature.

XII. CONCLUSION

Ferromagnetic materials were prepared with Binder Jet Printing and magnetically characterized with the Ring Specimen testbed, the Epstein Frame, and the Permeameter. The printing parameters for ferromagnetic materials, adapted from previous experience in printing high density stainless steels, are then analyzed using statistical analysis. It is found that both sintering temperature and the average particle size impact the maximum relative permeability of BJP ferromagnetic materials. The influence of sintering temperature on magnetic properties of BJP ferromagnetic materials draws similarity to the influence of laser power on magnetic properties of printed ferromagnetic materials using non-BJP processes. Based on the collected results, the influences of the two printing parameters, sintering temperature and average particle size, on the magnetic properties of the ferromagnetic materials are independent from each other. This finding is important since the impact of each of the two printing parameters on maximum relative permeability can be researched independently.

REFERENCES

[1] A. Krings, A. Boglietti, A. Cavagnino, and S. Sprague, "Soft magnetic material status and trends in electric machines," *IEEE Transactions on Industrial Electronics*, vol. 64, no. 3, pp. 2405–2414, March 2017.

[2] G. Cipriani, V. D. Dio, V. Franzitta, A. Russo, M. Trapanese, and A. Viola, "A ferrite tubular linear permanent magnet generator (ftlpmg) analysis and design," in *2014 Oceans - St. John's*, Sept 2014, pp. 1–6.

[3] J. Wang, M. West, D. Howe, H. Z. D. L. Parra, and W. M. Arshad, "Design and experimental verification of a linear permanent magnet generator for a free-piston energy converter," *IEEE Transactions on Energy Conversion*, vol. 22, no. 2, pp. 299–306, June 2007.

[4] C. W. Kim, G. H. Jang, J. M. Kim, J. H. Ahn, C. H. Baek, and J. Y. Choi, "Comparison of axial flux permanent magnet synchronous machines with electrical steel core and soft magnetic composite core," *IEEE Transactions on Magnetics*, vol. 53, no. 11, pp. 1–4, Nov 2017.

[5] W. R. Jensen, T. Q. Pham, and S. N. Foster, "Linear permanent magnet synchronous machine for high acceleration applications," in *2017 IEEE International Electric Machines and Drives Conference (IEMDC)*, May 2017, pp. 1–8.

[6] A. Schoppa and P. Delarbre, "Soft magnetic powder composites and potential applications in modern electric machines and devices," *IEEE Transactions on Magnetics*, vol. 50, no. 4, pp. 1–4, April 2014.

[7] R. Kobler, D. Andessner, G. Weidenholzer, and W. Amrhein, "Development of a compact and low cost axial flux machine using soft magnetic composite and hard ferrite," in *2015 IEEE 11th International Conference on Power Electronics and Drive Systems*, June 2015, pp. 810–815.

[8] R. Z. Haddad, S. N. Foster, E. G. Strangas, and Y. King, "Performance analysis of radial and axial flux fractional horsepower motors," in *2016 XXII International Conference on Electrical Machines (ICEM)*, Sept 2016, pp. 526–530.

[9] A. Ellery, "Progress towards 3d-printed mechatronic systems," in *2016 IEEE International Conference on Industrial Technology (ICIT)*, March 2016, pp. 1129–1133.

[10] E. Aguilera, J. Ramos, D. Espalin, F. Cedillos, D. Muse, R. Wicker, and E. MacDonald, "3d printing of electro mechanical systems," in *International Solid Freeform Fabrication Symposium, 2013 International Conference*, Aug 2013, pp. 950–961.

[11] M. Garibaldi, I. Ashcroft, M. Simonelli, and R. Hague, "Metallurgy of high-silicon steel parts produced using selective laser melting," *Acta Materialia*, vol. 110, pp. 207 – 216, 2016. [Online]. Available: http://www.sciencedirect.com/science/article/pii/S1359645416301902

[12] B. Zhang, N.-E. Fenineche, L. Zhu, H. Liao, and C. Coddet, "Studies of magnetic properties of permalloy (fe–30technology," *Journal of Magnetism and Magnetic Materials*, vol. 324, no. 4, pp. 495 – 500, 2012. [Online]. Available: http://www.sciencedirect.com/science/article/pii/S0304885311005932

[13] L. Li, B. Post, V. Kunc, A. M. Elliott, and M. P. Paranthaman, "Additive manufacturing of near-net-shape bonded magnets: Prospects and challenges," *Scripta Materialia*, pp. –, 2017. [Online]. Available: http://www.sciencedirect.com/science/article/pii/S1359646216306352

[14] R. Hilzinger and W. Rodewald, *Magnetic Materials*. Wiley, 2013. [Online]. Available: https://books.google.at/books?id=uAiquAAACAAJ

[15] M. Bali, "Magnetic material degradation due to different cutting techniques and its modeling for electric machine design," Ph.D. dissertation, Technischen Universität Graz, Graz, Austria, 2016.

[16] M. Vaezi, S. Chianrabutra, B. Mellor, and S. Yang, "Multiple material additive manufacturing – part 1: a review," *Virtual and Physical Prototyping*, vol. 8, no. 1, pp. 19–50, 2013. [Online]. Available: https://doi.org/10.1080/17452759.2013.778175

[17] Z.-Y. Zhang, M.-C. Tsai, P.-W. Huang, C.-W. Cheng, and J.-M. Huang, "Characteristic comparison of transversally laminated anisotropic synchronous reluctance motor fabrication based on 2d lamination and 3d printing," in *Electrical Machines and Systems (ICEMS), 2015 18th International Conference on*, Oct 2015, pp. 894–897.

[18] Z. Y. Zhang, K. J. Jhong, C. W. Cheng, P. W. Huang, M. C. Tsai, and W. H. Lee, "Metal 3d printing of synchronous reluctance motor," in *2016 IEEE International Conference on Industrial Technology (ICIT)*, March 2016, pp. 1125–1128.

[19] G.-M. Tseng, M.-C. Tsai, P.-W. Huang, and W.-H. Lee, "A radially inserted permanent-magnet magnetic coupling design based on 3d printing," in *Electrical Machines and Systems (ICEMS), 2015 18th International Conference on*, Oct 2015, pp. 973–976.

[20] H. Y. Jung, S. J. Choi, K. G. Prashanth, M. Stoica, S. Scudino, S. Yi, U. Kühn, D. H. Kim, K. B. Kim, and J. Eckert, "Fabrication of fe-based bulk metallic glass by selective laser melting: A parameter study," *Materials & Design*, vol. 86, pp. 703 – 708, 2015. [Online]. Available: http://www.sciencedirect.com/science/article/pii/S0264127515302148

[21] R. Conteri, T. Borkar, S. Nag, D. Jaeger, X. Chen, R. Ramanujan, and R. Banerjee, "Laser additive processing of fe-si-b-cu-nb magnetic alloys," *Journal of Manufacturing Processes*, vol. 29, pp. 175 – 181, 2017. [Online]. Available: http://www.sciencedirect.com/science/article/pii/S1526612517302311

[22] T. Borkar, R. Conteri, X. Chen, R. V. Ramanujan, and R. Banerjee, "Laser additive processing of functionally-graded fe–si–b–cu–nb soft magnetic materials," *Materials and Manufacturing Processes*, vol. 0, no. 0, pp. 1–7, 0. [Online]. Available: http://dx.doi.org/10.1080/10426914.2016.1244849

[23] M. Lindner, P. Bräuer, and R. Werner, "Increasing the torque density of permanent-magnet synchronous machines using innovative materials and winding technologies," in *Systems, Signals and Devices (SSD), 2012 9th International Multi-Conference on*, March 2012, pp. 1–7.

[24] M. Lindner and R. Werner, "Hysteresis-model oriented test procedure for soft-magnetic properties of printed or laminated toroids," in *Electric Drives Production Conference (EDPC), 2014 4th International*, Sept 2014, pp. 1–8.

[25] A. B. Kustas, D. F. Susan, K. L. Johnson, S. R. Whetten, M. A. Rodriguez, D. J. Dagel, J. R. Michael, D. M. Keicher, and N. Argibay, "Characterization of the fe-co-1.5v soft ferromagnetic alloy processed by laser engineered net shaping (lens)," *Additive Manufacturing*, vol. 21, pp. 41 – 52, 2018. [Online]. Available: http://www.sciencedirect.com/science/article/pii/S2214860417306103

[26] J. Geng, I. C. Nlebedim, M. F. Besser, E. Simsek, and R. T. Ott, "Bulk combinatorial synthesis and high throughput characterization for rapid assessment of magnetic materials: Application of laser engineered net shaping (lens$^{\text{TM}}$)," *JOM*, vol. 68, no. 7, pp. 1972–1977, Jul 2016. [Online]. Available: https://doi.org/10.1007/s11837-016-1918-x

[27] [Online]. Available: https://www.vacuumschmelze.com/index.php?id=117

[28] C. Mikler, V. Chaudhary, V. Soni, B. Gwalani, R. Ramanujan, and R. Banerjee, "Tuning the phase stability and magnetic properties of laser additively processed fe-30at199, pp. 88 – 92, 2017. [Online]. Available: http://www.sciencedirect.com/science/article/pii/S0167577X17305992

[29] B. Zhang, N.-E. Fenineche, H. Liao, and C. Coddet, "Magnetic properties of in-situ synthesized feni3 by selective laser melting fe-80*Journal of Magnetism and Magnetic Materials*, vol. 336, pp. 49 – 54, 2013. [Online]. Available: http://www.sciencedirect.com/science/article/pii/S0304885313000966

[30] X. Wang, M. Wraith, S. Burke, H. Rathbun, and K. DeVlugt, "Densification of w–ni–fe powders using laser sintering," *International Journal of Refractory Metals and Hard Materials*, vol. 56, pp. 145 – 150, 2016. [Online]. Available: http://www.sciencedirect.com/science/article/pii/S0263436815302626

[31] B. Zhang, N.-E. Fenineche, H. Liao, and C. Coddet, "Microstructure and magnetic properties of fe–ni alloy fabricated by selective laser melting fe/ni mixed powders," *Journal of Materials Science & Technology*, vol. 29, no. 8, pp. 757 – 760, 2013. [Online]. Available: http://www.sciencedirect.com/science/article/pii/S1005030213001205

[32] I. Shishkovsky and V. Saphronov, "Peculiarities of selective laser melting process for permalloy powder," *Materials Letters*, vol. 171, pp. 208 – 211, 2016. [Online]. Available: http://www.sciencedirect.com/science/article/pii/S0167577X16302567

[33] C. Mikler, V. Chaudhary, T. Borkar, V. Soni, D. Choudhuri, R. Ramanujan, and R. Banerjee, "Laser additive processing of ni-fe-v and ni-fe-mo permalloys: Microstructure and magnetic properties," *Materials Letters*, vol. 192, pp. 9 – 11, 2017. [Online]. Available: http://www.sciencedirect.com/science/article/pii/S0167577X1730068X

[34] Y. Sato and T. Takeyama, "Magnetic and mechanical properties of a 6permalloy as magnetic head materials," *Journal of the Japan Institute of Metals*, vol. 46, no. 11, pp. 1089–1094, 1982.

[35] K. J. Jhong, W.-C. Huang, and W. H. Lee, "Microstructure and magnetic properties of magnetic material fabricated by selective laser melting," *Physics Procedia*, vol. 83, pp. 818 – 824, 2016, laser Assisted Net Shape Engineering 9 International Conference on Photonic Technologies Proceedings of the LANE 2016 September 19-22, 2016

Fürth, Germany. [Online]. Available: http://www.sciencedirect.com/science/article/pii/S1875389216301912

[36] S. Lammers, G. Adam, H. J. Schmid, R. Mrozek, R. Oberacker, M. J. Hoffmann, F. Quattrone, and B. Ponick, "Additive manufacturing of a lightweight rotor for a permanent magnet synchronous machine," in *2016 6th International Electric Drives Production Conference (EDPC)*, Nov 2016, pp. 41–45.

[37] M. Garibaldi, I. Ashcroft, N. Hillier, S. Harmon, and R. Hague, "Relationship between laser energy input, microstructures and magnetic properties of selective laser melted fe-6.9%wt si soft magnets," *Materials Characterization*, 2018. [Online]. Available: http://www.sciencedirect.com/science/article/pii/S1044580317331674

[38] T. Q. Pham, T. T. Do, P. Kwon, and S. N. Foster, "Additive manufacturing of high performance ferromagnetic materials," (in press).

[39] D. D. Gu, W. Meiners, K. Wissenbach, and R. Poprawe, "Laser additive manufacturing of metallic components: materials, processes and mechanisms," *International Materials Reviews*, vol. 57, no. 3, pp. 133–164, 2012. [Online]. Available: http://dx.doi.org/10.1179/1743280411Y.0000000014

[40] L. E. Murr, E. Martinez, K. N. Amato, S. M. Gaytan, J. Hernandez, D. A. Ramirez, P. W. Shindo, F. Medina, and R. B. Wicker, "Fabrication of metal and alloy components by additive manufacturing: Examples of 3d materials science," *Journal of Materials Research and Technology*, vol. 1, no. 1, pp. 42 – 54, 2012. [Online]. Available: http://www.sciencedirect.com/science/article/pii/S2238785412700091

[41] Y. Yan, K. D. T. Ngo, Y. Mei, and G.-Q. Lu, "Additive manufacturing of magnetic components for power electronics integration," in *2016 International Conference on Electronics Packaging (ICEP)*, April 2016, pp. 368–371.

[42] G. Manogharan, M. Kioko, and C. Linkous, "Binder jetting: A novel solid oxide fuel-cell fabrication process and evaluation," *JOM*, vol. 67, no. 3, pp. 660–667, Mar 2015. [Online]. Available: https://doi.org/10.1007/s11837-015-1296-9

[43] T. Do, C. Shin, D. Stetsko, G. Vanconant, A. Vartanian, S. Pei, and P. Kwon, "Improving structural integrity with boron-based additives for 3d printed 420 stainless steel," *Procedia Manufacturing*, vol. 1, pp. 263–272, 1 2015.

[44] T. Do, P. Kwon, and C. Shin, "Process development toward full-density stainless steel parts with binder jetting printing," *International Journal of Machine Tools and Manufacture*, 11 2016.

[45] *Magnetic materials - Part 6: Methods of measurement of the magnetic properties of magnetically soft metallic and powder materials at frequencies in the range 20 Hz to 200 kHz by the use of ring specimens*, International Std. IEC 60 404-6, 2003.

[46] *Magnetic materials - Part 4: Methods of measurement of d.c. magnetic properties of magnetically soft materials*, International Std. IEC 60 404-4, 2008.

[47] *Magnetic materials - Part 2: Methods of measurement of the magnetic properties of electrical steel strip and sheet by means of an Epstein frame*, International Std. IEC 60 404-2, 2008.

[48] *Magnetic materials - Part 10: Methods of measurement of magnetic properties of electrical steel strip and sheet at medium frequencies*, International Std. IEC 60 404-10, 1988.

[49] S. Tumanski, *Handbook of Magnetic Measurements*, ser. Series in Sensors. CRC Press, 2016. [Online]. Available: https://books.google.at/books?id=s0npF4E5jasC

[50] [Online]. Available: https://cogent-power.com/cms-data/downloads/m600-50a.pdf

[51] [Online]. Available: https://cogent-power.com/cms-data/downloads/m800-50a.pdf

[52] [Online]. Available: https://www.hoganas.com/globalassets/media/sharepoint-documents/BrochuresanddatasheetsAllDocuments/Somaloy_Prototyping_Material_May_2015_1058HOG.pdf

[53] G. Bertotti, "Some considerations on the physical interpretation of eddy current losses in ferromagnetic materials," *Journal of Magnetism and Magnetic Materials*, vol. 54-57, pp. 1556 – 1560, 1986. [Online]. Available: http://www.sciencedirect.com/science/article/pii/0304885386909261

[54] D. C. Montgomery, *Design and Analysis of Experiments*. USA: John Wiley & Sons, Inc., 2006.